Ferrobotic swarms enable accessible and adaptable automated viral testing
Haisong Lin ^{1,4} , Wenzhuo Yu ^{1,4} , Kiarash A. Sabet ^{1,4} , Michael Bogumil ² , Yichao Zhao ¹ , Jacob Hambalek ² ,
Shuyu Lin ¹ , Sukantha Chandrasekaran ³ , Omai Garner ³ ,
Dino Di Carlo ^{2□} , and Sam Emaminejad ^{1,2□}
¹ Department of Electrical and Computer Engineering, UCLA
² Department of Bioengineering, UCLA
³ Department of Pathology and Laboratory Medicine, UCLA
⁴ These authors contributed equally: Haisong Lin, Wenzhuo Yu, Kiarash A. Sabet
e-mail: dicarlo@ucla.edu; emaminejad@ucla.edu

Abstract

Expanding our global testing capacity is critical to preventing and containing pandemics^[1-9]. Accordingly, accessible and adaptable automated platforms that in decentralized settings perform nucleic acid amplification tests (NAATs) resource-efficiently are required^[10-14]. Pooled testing can be extremely efficient if the pooling strategy is based on local viral prevalence^[15-20]—but it requires automation, small sample volume handling, and feedback not available in current bulky, capital-intensive liquid handling technologies^[21-29]. Overcoming these limitations, here, we employ a swarm of millimeter-sized magnets as mobile robotic agents ("ferrobots") for precise and robust handling of magnetized sample droplets and highfidelity delivery of flexible NAAT-based workflows. Accordingly, within a palm-sized printed circuit board-based programmable platform, we demonstrated the myriad of lab-equivalent operations involved in pooled testing. These operations were guided by an introduced square matrix pooled testing algorithm to identify the infected patient samples, while maximizing the testing efficiency. We applied this automated technology for the loop-mediated isothermal amplification and detection of SARS-CoV-2 virus in clinical samples, where the test results completely matched those obtained off-chip. This technology is easily manufacturable and distributable, and its adoption for viral testing could lead to a 10-to-300-fold reduction in reagent costs (depending on the viral prevalence), and three orders of magnitude reduction in instrumentation cost. Therefore, it is a promising solution to expand our testing capacity for pandemic preparedness and to re-imagine the automated clinical lab of the future.

Main

Over the past two decades, major epidemics (SARS, Zika, MERS, and Ebola) and pandemics (H1N1 and COVID-19) have emerged with increasingly alarming regularity^[1-3]. Although currently the world is grappling with the COVID-19 pandemic, the occurrence of the next wave of infectious disease outbreaks in the coming years is deemed inevitable, given the rise in population, urbanization, and global travel/trade. In that regard, large-scale population screening is the primary safeguard to contain epidemics, prevent pandemics, and mitigate their human and economic costs upon their onset^[4-6].

Accordingly, increasing our viral diagnostic and surveillance testing capacity globally is fundamental to our epidemic/pandemic preparedness^[7-9]. Among the test options, nucleic acid amplification tests (NAATs) are advantageous over the antigen- and antibody-based counterparts, owing to their superior sensitivity, specificity, and ability for rapid deployment without the need to generate specific diagnostic antibodies^[10,11]. To perform NAATs at large scale and frequency, accessible automated testing platforms are required that can be deployed in decentralized settings to analyze samples with high throughput, fast turnaround time, and minimal capital cost/reagent use^[12-14]. In particular, the strategic pooling of samples^[15-18], when most patients are expected to be negative, can lead to a dramatic reduction in resource utilization amid pandemic-induced supply chain disruptions (outweighing the marginal risk of dilution-induced false negatives^[19,20]). Accordingly, flexible testing workflows dictated by adaptive pooling algorithms—such as viral prevalence-based ones—that are intended to maximize the screening efficiency are needed (Fig. 1a,b).

However, current automated NAAT-based testing platforms are unable to perform the integrated liquid handling, analysis, and automated feedback processes necessary to achieve these flexible workflows^[21-23]. Additionally, they employ bulky, expensive, and reagent-wasteful robotic liquid handlers and bioinstruments, with heavy installations and maintenance needs, and thus, they are restricted to centralized laboratory settings^[24-29].

To enable adaptive pooled testing, here, we created an automated NAAT-based testing platform, which performs programmable liquid handling and bioanalytical operations within flexible workflows and in a parallel manner. Instead of resource-intensive, and functionally-limited robotic liquid handlers, we employed a swarm of individually-addressable millimeter-sized magnets as mobile robotic agents ("ferrobots") that can manipulate magnetic nanoparticle-spiked droplets ("ferro-droplets") with high precision and robustness. The seamless integration of fluidware, hardware, and software allowed for programing and streamlining the droplet-based operations, and delivering versatile automated NAAT-centered workflows within a compact platform (e.g., here we implemented reverse transcription loop mediated isothermal amplification, RT-LAMP). To maximize the screening efficiency, we formulated a prevalence-based adaptive testing algorithm (Fig. 1b, Supplementary Note 1). This algorithm particularly determines the optimal testing mode and guides the operational workflow in accordance with a square

matrix pooling scheme (Fig. 1c,d), without entailing overly burdensome sample handling procedures. Adopting this approach over the fixed individual testing approach (universally pursued) allows for significant savings over a wide viral prevalence range.

Figure 1e-g illustrates a representative ferrobotic testing platform, which consists of two modules (entirely constructed by low-cost components): 1) a disposable oil-filled microfluidic chip with passive and active actuation interfaces that hosts input sample(s) and ferrofluid/assay reagents and 2) a printed circuit board (PCB), featuring 2D arrayed coils ("navigation floor"), which can be independently activated to electromagnetically direct individual ferrobots.

We realized the miniaturized bioanalytical operations and workflows within the framework of ferrobotics, because it simultaneously offers high degrees of robustness, diversity, programmability, and scalability for low-volume sample handling. Within this framework, we developed and characterized a suite of operations, including droplet transportation, aliquoting, merging, mixing, and heating, which are key to the on-chip implementation of NAAT-based assays (Fig. 2, Extended Data Fig. 1).

By programming the underlying PCB-based coils, we electromagnetically directed the ferrobots to carry ferro-droplets within different oil environments, where rapid droplet transportation with a maximum velocity range of 5-50 mm/s was achieved (Fig. 2a, Extended Data Fig. 1b). We found that Novec (oil)/Picosurf (surfactant) yielded the maximum ferro-droplet speed (owing to its low viscosity, Supplementary Note 2), while being compatible with the RT-LAMP assay.

Figure 2b illustrates the precise and tunable ferrobotic sample aliquoting capability in the optimized Novec oil environment. In our context, aliquoting is a critical step for precise sample metering and creating sub-samples for multiplexing and multi-round pooling analysis. Aliquoting is achieved by directing a ferrodroplet-carrying ferrobot along a corrugated structural feature, which in turn causes the dispensing of a smaller ferro-droplet (as an aliquot). By adjusting the corrugation opening and/or the channel height, the volume of the aliquot could be tuned over two orders of magnitude (*e.g.*, here 100 nL-10 μL; Extended Data Fig. 1c,d and Extended Data Fig. 2a).

To realize droplet merging, we utilized the principle of electrocoalescence. In our context, droplet merging is useful for adding reagent(s) to the input sample(s) and combining multiple input samples for pooling. As shown in Fig. 2c, by transporting the droplets to an electrode pair and applying a relatively low voltage (~0.3 V - 1.5 V, depending on the surrounding oil surfactant composition, Supplementary Note 3) droplet merging in less than a few seconds can be achieved.

We found that robust and repeatable ferrobotic droplet actuation can be achieved for droplets spanning different ionic strengths and chemical compositions relevant for biological and chemical assays (Extended Data Fig. 3). A total of > 8 million actuation events were performed over > 24 h (only limited by the observation time) showing repeatable behavior over the time period. This behavior differs from

common digital microfluidics approaches such as electrowetting on dielectric (EWOD), which undergo surface degradation-related issues^[30-32]. Further illustrating that other ferrobotic operations are robust, we performed cyclic aliquoting, merging, and intermediate transportation of a parent droplet over 800 cycles with < 1% variation in the corresponding size of the parent droplet post-aliquoting and post-merging (Fig. 2d).

97

98

99 100

101

102

103

104

105

106

107

108

109

110

111

112

113

114

115

116

117

118

119

120

121

122

123

124

125

126

127

128

129

To realize mixing, which is particularly important for homogenizing the droplet contents postmerging, the ferrobot can be oscillated to induce chaotic fluid motion within the merged droplet by alternatively activating the neighboring coils. As shown in Fig. 2e, the droplet homogenization rate increases with oscillation frequency, and in particular, a nearly full-mixed state can be reached in ~15 seconds by oscillating the ferrobot at 5 Hz.

We used on-board resistive heaters for nucleic acid amplification and sample preparation (*e.g.*, lysis). The local temperature can be controlled by adjusting the DC current flowing through the resistive heater, in accordance with the operational needs (Fig. 2f and Extended Data Fig. 4a-c).

We implemented a colorimetric RT-LAMP assay that is based on thermal lysis/inactivation^[21] and isothermal amplification (both achievable with on-board resistive heaters). This assay provides a high degree of test accessibility, outweighing the marginal compromise in test accuracy^[19,20]. Figure 2g illustrates the RT-LAMP reactions, which involve the reverse transcription of the viral RNA, amplification of the product DNA, and generation of hydrogen ions, which are colorimetrically detected. By analyzing the reaction product (DNA) via gel electrophoresis (Fig. 2h and Supplementary Fig. 1), we verified the assay function in converting and amplifying a severe acute respiratory syndrome coronavirus 2 (SARS-CoV-2) positive control RNA sample. Colorimetric detection is based on the generated hydrogen ions, causing a color change of an incorporated pH indicator (phenol red) from red-orange to yellow (optimization experiment results shown in Extended Data Fig. 5a-c). The color change allows for the binary interpretation of the test, above or below a threshold as positive or negative, respectively. This color change can be tracked visually (Fig. 2i) by the naked eye, or electronically by integrating an optical sensor (Fig. 2j and Extended Data Fig. 4b,d), without the absorbance of the ferrofluid affecting the readout interpretations. Accordingly, the same limit of detection of 25 cp/µL of the adopted assay [33] can be achieved in the ferrodroplet format (1 μL; reagent volume 19 μL; similar to the original assay protocol), suggesting the magnetic nanoparticles do not interfere with the amplification chemistry or colorimetric readout accuracy (Extended Data Fig. 5d). The assay was also successfully performed by using microfluidic structures of reduced height (~150 μm) to aliquot a 10-fold smaller ferro-droplet volume (100 nL; reagent volume 1.9 μL; Extended Data Fig. 5e), which is below the volume that can be accurately pipetted using robotic liquid handlers, but useful for minimizing reagent use. Our characterization results also verified the reliability of the assay in

the presence of temperature variations of a few degrees Celsius (Supplementary Fig. 2a) and in the presence of biological interferents (Supplementary Fig. 3).

Our platform's programmability (Supplementary Figure 4) allows for its ease of adaptation to streamline the ferrobotic actuation and bioanalytical operations and deliver versatile RT-LAMP-based testing workflows in an entirely automated fashion and with high fidelity.

Illustrating this point in the context of individual sample testing, we customized a disposable microfluidic module to host the input sample, associated reagents, and dedicated aliquoting/merging components (Fig. 3a, Extended Data Fig. 4b)—then, augmented it with a PCB module, containing the navigation coils, resistive heater elements, and colorimetric sensing circuitry. By programming the PCB at the software-level, we installed a ferrobotic instruction set to seamlessly execute the assay. The instruction set charts the navigation plan of a dedicated ferrobot and details the electrode excitation conditions for merging and heating, while accounting for a 5 min-heat lysis and a 30-min RT-LAMP reaction period (Fig. 3b).

In this testing workflow, the active ferrobotic operations take place over a period of 1.75 minutes (Fig. 3c, Supplementary Video 1). A ferro-droplet is first magnetically transported to, then merged and mixed with an introduced sample droplet, in order to make the sample amenable for ferrobotic manipulation. The next steps in the sequence are aliquoting the ferro-sample, disposing the ferro-sample residue, and delivering the aliquot (1 μL) to the reaction chamber (containing the assay reagents). Upon delivery to the reaction chamber, the RT-LAMP process initiates, and after 30 min, the assay readout is colorimetrically quantified, rendering the test result in a sample-to-answer manner. A similar workflow was implemented using microfluidic chips with reduced height to achieve smaller ferro-droplets (~100 nL) for analysis with reduced reagents (Extended Data Fig. 2b).

We assessed the accuracy of our platform with real world samples by testing one hundred clinical samples with the ferrobotic RT-LAMP chip, and comparing the on-chip readouts with the corresponding readouts obtained from the standard RT-PCR and RT-LAMP assays (summarized in Fig. 3d, detailed in Supplementary Table 6). The collected samples were based on nasopharyngeal swabs from SARS-CoV-2 infected or uninfected patients. The viral on-chip detection threshold (710 a.u.) was derived from receiver operating characteristic (ROC) analysis (aliquoted sample volume: 1 µL).

For all one hundred samples, the ferrobotically produced results were in agreement with the manually performed (off-chip) RT-LAMP assay results (100% concordance), illustrating the high fidelity of the ferrobotic automation. Comparison of the ferrobotically produced RT-LAMP-based results with the corresponding results obtained from the RT-PCR assay (gold standard) resulted in a test sensitivity of 98% and specificity of 100% (Fig. 3e), wherein the rare test result discrepancy can be attributed to the inherent differences of the employed amplification approaches^[33]. We further validated that the clinical samples

with aliquoted volumes of 1 μ L and 100 nL can be accurately analyzed in a reproducible manner across replicates (Extended Data Fig. 6).

We next demonstrated multiplexed viral testing by utilizing our platform's adaptability (Extended Data Fig. 7, Supplementary Video 2, Supplementary Note 4). This testing mode is diagnostically useful for differentiating between the emergent outbreak virus (*e.g.*, SARS-CoV-2) and endemic viruses (*e.g.*, the seasonal ones such as influenza A–H1N1) that often result in similar clinical symptoms^[34-37].

By utilizing the platform's scalability, we can increase the testing throughput. The extensibility of the employed mobile robotic scheme to a multi-agent mobile (swarm) robotic scheme, together with the expandability of the navigation floor/microfluidic architecture, inherently render our platform scalable. One approach to increasing the throughput is to simply extend our individual testing platform into an array format (Extended Data Fig. 4a,e). With this implementation, a large number of input samples can be analyzed in parallel and asynchronously as they arrive—without involving accumulation wait time (unlike the case for current high throughput methods that rely on batch-processing^[38]). A less trivial, yet more efficient high throughput testing approach involves applying our platform to the problem of adaptive pooled testing.

To determine the appropriate number of input samples and guide the pooled testing workflow, we utilized our prevalence-based adaptive testing algorithm that can be implemented following a square matrix pooling scheme. Following this approach, testing efficiency can be substantially improved in moderate-to-low viral prevalence ranges (specifically, by appropriately performing 3² or 4² matrix pooling, determined algorithmically, Supplementary Note 1).

Figure 4a provides an overview of the algorithm-guided square matrix pooling scheme, particularly for the case of 4^2 pooling, which involves a group of 16 samples arranged in a 4×4 matrix (S_{ij} , i,j represent the row and column indices, respectively). In this scheme, all the samples are first pooled together and the resultant sample aggregate will be analyzed by a single assay "A". If the assay readout is negative, all the original input samples will be deemed negative. Otherwise, a second round of testing will be followed. In this round, the samples will be pooled along rows and columns, leading to a total of eight sample aggregates. The row-pooled and column-pooled sample aggregates will be correspondingly analyzed by dedicated " R_i " and " C_j " assays. The intersectional analysis of the R_i and C_j assay readouts allows for determining the infected sample(s) (Supplementary Fig. 5 and Fig. 1d). In the relatively low probable cases (*e.g.*, 2.5%, assuming the viral prevalence of 2%) where the paired row/column projections are not one-to-one mapped to specific arrangements of multiple positive samples, only those samples that are deemed suspicious (*i.e.*, those located at the intersection of positive row/column projections) will be individually tested.

To implement the square matrix pooled testing workflow, we expanded the microfluidic chip layout for pooled testing. Extended Data Fig. 8a,b illustrates the corresponding layouts of the 3² and 4² microfluidic

chips. The expanded layouts especially include arrays of sample aliquoting interfaces and reaction chambers (containing SARS-CoV-2 RT-LAMP assay solutions), orthogonal corridors for intra-chip sample aliquot transport, and extended merging interfaces. To direct the swarm ferrobotic operations in accordance with the devised pooling scheme, we utilized a PCB module with increased navigation coils (*i.e.*, an expanded navigation floor) and programmed the PCB module to install an updated multi-ferrobot-based and pooling algorithm-driven instruction set.

Figure 4b and Supplementary Video 3 illustrate the sequence of the operations performed by a swarm of nine ferrobots to deliver a representative 4^2 pooled testing workflow. The demonstrated sequence involves: 1) making three aliquots of each input samples with the aid of four ferrobots; 2) all-sample pooling to facilitate the first round of testing (performed in two steps; combining the aliquots on the same row using four ferrobots in parallel, followed by combining the resultant aggregates using a single ferrobot); and 3) row/column pooling to facilitate the second round of testing (each performed by a set of four ferrobots). To combine the intended aliquots in each of the pooling steps, the aliquots were ferrobotically collected, merged, mixed, and then dispensed as a droplet with a metered volume (1 μ L). The overview of the navigation plan and the detailed timeline of the task sequence executed by each ferrobot (in coordination with the other ferrobots) are illustrated in Extended Data Fig. 8c-f.

Prior to applying the scaled platform for pooled testing of clinical samples, we evaluated the dilutive effect of sample pooling on the assay detection capability (using positive nasal swab samples). The results indicated the assay capability in correctly identifying positive samples with a relatively low viral load, even at dilutions as high as 16 times (Extended Data Fig. 9).

We examined the pooled testing capability of the scaled platform by analyzing a collection of fifty clinical samples (pre-characterized *via* RT-PCR). These samples were grouped in two arrangements of 9 and 16 samples and tested with the corresponding 3^2 and 4^2 chips in a way to allow for evaluating the platform's pooling, detection, and interpretation capabilities in the first and second rounds of testing. Specifically, for each group size/chip, we tested the scenarios that involved the absence or the presence of an infected sample. Figures 4c-f illustrate the corresponding on-chip optical characterization results (with assay reagent volumes of 19 μ L to analyze aliquoted samples with volumes of 1 μ L). Following the aforementioned testing scheme, by comparing the corresponding assay responses (all-pooled, A or row/column-pooled, R_i/C_j) with respect to their detection threshold, we determined the status of each sample. We performed similar pooled testing studies using smaller aliquoted samples (100 nL, with assay reagent volumes of 1.9 μ L), demonstrating the ability to reduce reagents further (Extended Data Fig. 10). For all tested scenarios and across all samples, the ferrobotically produced/interpreted results were inline with those obtained by RT-PCR.

The demonstrated pooled-testing application, and scale of microfluidic liquid handling operations, is unprecedented. Supplementary Table 1 provides a detailed account of the number of droplet actuation and ferrobotic operations that were reliably carried out to achieve pooled testing. This was achieved by harnessing the competitive advantages of the ferrobotic technology that overcomes performance limits (in terms of reliability, scalability, reagent use, portability *etc.*) and cost barriers of alternative microfluidics approaches (Supplementary Note 5).

231

232

233

234

235

236

237

238

239

240

241

242

243

244

245

246

247

248

249

250

251

252

253

Depending on the situational needs, the ferrobotic testing platform can be adapted—with minimal reconfiguration—to automate other NAAT-based assays (e.g., RT-PCR) as well as other pooling schemes (e.g., Dorfman^[39]). The ferrobotic testing platform can be constructed with low-cost consumables (Supplementary Table 2) and instrumentation (Supplementary Table 3) using widely available materials and circuit components and following existing scalable manufacturing solutions—altogether enabling mass-production for rapid large-scale deployment. As summarized in Supplementary Table 4, we estimate that translating this platform for population-level screening can ultimately lead to ~3 orders of magnitude of increase in marginal gain in testing capacity from the instrumentation investment standpoint, and a 60 to 300-fold reduction in reagent costs at moderate-to-low viral prevalence (~8 to 0.8%) and 10-fold reduction at high viral prevalence. Accordingly, utilizing its high level of accessibility, adaptability, and automation, the presented technology can be deployed as a democratized, distributed, and decentralized solution to expand our testing capacity for pandemic preparedness. Beyond viral testing, the presented swarm ferrobotic technology can be adapted and scaled to efficiently streamline and massively parallelize a variety of other lab-based bioanalytical operations within a miniaturized footprint (Supplementary Note 6). Thus, this technology can serve as a powerful tool for a wide range of biomedical and biotechnological applications such as diagnostics, omics, drug development, and chemical/biomaterial synthesis.

254 References:

- 255 1. Zhu, H. et al. The vision of point-of-care PCR tests for the COVID-19 pandemic and beyond.
- 256 Trends Analyt. Chem. 130, 115984 (2020).
- 257 2. Zhuang, J., Yin, J., Lv, S., Wang, B. & Mu, Y. Advanced 'lab-on-a-chip' to detect viruses Current
- challenges and future perspectives. *Biosens. Bioelectron.* **163**, 112291 (2020).
- 3. Sands, P., Mundaca-Shah, C. & Dzau, V. J. The Neglected Dimension of Global Security--A
- Framework for Countering Infectious-Disease Crises. N. Engl. J. Med. 374, 1281–1287 (2016).
- 4. Weissleder, R., Lee, H., Ko, J. & Pittet, M. J. COVID-19 diagnostics in context. Science
- *Translational Medicine* vol. 12 (2020).
- 5. Mercer, T.R., Salit, M. Testing at scale during the COVID-19 pandemic. Nat Rev Genet 22, 415–
- 264 426 (2021).
- 6. Patchsung, M. et al. Clinical validation of a Cas13-based assay for the detection of SARS-CoV-2
- 266 RNA. *Nat Biomed Eng* **4**, 1140–1149 (2020).
- 7. Vandenberg, O., Martiny, D., Rochas, O. et al. Considerations for diagnostic COVID-19 tests. Nat
- 268 Rev Microbiol 19, 171–183 (2021).
- 8. Cheong, J., Yu, H., Lee, C.Y. et al. Fast detection of SARS-CoV-2 RNA via the integration of
- plasmonic thermocycling and fluorescence detection in a portable device. *Nat Biomed Eng* **4**, 1159–
- 271 1167 (2020).
- 9. Ramachandran, A. et al. Electric field-driven microfluidics for rapid CRISPR-based diagnostics
- and its application to detection of SARS-CoV-2. Proc. Natl. Acad. Sci. U. S. A. 117, 29518–29525
- 274 (2020).
- 275 10. Simpson, S., Kaufmann, M. C., Glozman, V. & Chakrabarti, A. Disease X: accelerating the
- development of medical countermeasures for the next pandemic. *Lancet Infect. Dis.* **20**, e108–e115
- 277 (2020).
- 11. Mardian, Y., Kosasih, H., Karyana, M., Neal, A. & Lau, C.-Y. Review of Current COVID-19

- Diagnostics and Opportunities for Further Development. Front. Med. 8, 615099 (2021).
- 280 12. Valera, E. et al. COVID-19 Point-of-Care Diagnostics: Present and Future. ACS Nano 15, 7899–
- **281** 7906 (2021).
- 282 13. Zhu, H., Fohlerová, Z., Pekárek, J., Basova, E. & Neužil, P. Recent advances in lab-on-a-chip
- technologies for viral diagnosis. *Biosens. Bioelectron.* **153**, 112041 (2020).
- 284 14. Asghari, A. et al. Fast, accurate, point-of-care COVID-19 pandemic diagnosis enabled through
- advanced lab-on-chip optical biosensors: Opportunities and challenges. Appl Phys Rev 8, 031313
- 286 (2021).
- 287 15. Mutesa, L. et al. A pooled testing strategy for identifying SARS-CoV-2 at low prevalence. Nature
- **589**, 276–280 (2021).
- 16. Kevadiya, B.D., Machhi, J., Herskovitz, J. et al. Diagnostics for SARS-CoV-2 infections. Nat.
- 290 *Mater.* **20**, 593–605 (2021).
- 291 17. Binnicker, M. J. Challenges and Controversies to Testing for COVID-19. J. Clin. Microbiol. 58,
- 292 (2020).
- 293 18. Barak, N. et al. Lessons from applied large-scale pooling of 133,816 SARS-CoV-2 RT-PCR tests.
- 294 Sci. Transl. Med. 13, (2021).
- 19. Larremore, D. B. et al. Test sensitivity is secondary to frequency and turnaround time for COVID-
- 296 19 screening. *Sci Adv* 7, (2021).
- 20. Habli, Z., Saleh, S., Zaraket, H. & Khraiche, M. L. COVID-19 Diagnostics: State-of-the-Art and
- 298 Challenges for Rapid, Scalable, and High-Accuracy Screening. Front Bioeng Biotechnol 8, 605702
- 299 (2020).
- 300 21. Smyrlaki, I. et al. Massive and rapid COVID-19 testing is feasible by extraction-free SARS-CoV-
- 301 2 RT-PCR. *Nat. Commun.* **11**, 4812 (2020).
- 302 22. Ganguli, A. *et al.* Rapid isothermal amplification and portable detection system for SARS-CoV-2.
- 303 *Proc. Natl. Acad. Sci. U. S. A.* 117, 22727–22735 (2020).
- 304 23. Sun, F. et al. Smartphone-based multiplex 30-minute nucleic acid test of live virus from nasal swab

- 305 extract. *Lab Chip* **20**, 1621–1627 (2020).
- 306 24. Lukas, H., Xu, C., Yu, Y. & Gao, W. Emerging Telemedicine Tools for Remote COVID-19
- 307 Diagnosis, Monitoring, and Management. *ACS Nano* **14**, 16180–16193 (2020).
- 308 25. Consortium, I. G. I. S.-C.-2 T. et al. Blueprint for a Pop-up SARS-CoV-2 Testing Lab.
- 309 doi:10.1101/2020.04.11.20061424.
- 310 26. Tymm, C., Zhou, J., Tadimety, A., Burklund, A. & Zhang, J. X. J. Scalable COVID-19 Detection
- Enabled by Lab-on-Chip Biosensors. *Cell. Mol. Bioeng.* 1–17 (2020).
- 27. Pfefferle, S., Reucher, S., Nörz, D. & Lütgehetmann, M. Evaluation of a quantitative RT-PCR assay
- for the detection of the emerging coronavirus SARS-CoV-2 using a high throughput system. *Euro*
- 314 surveillance: bulletin Europeen sur les maladies transmissibles = European communicable disease
- 315 *bulletin* vol. 25 (2020).
- 316 28. Karp, D. G. et al. Sensitive and Specific Detection of SARS-CoV-2 Antibodies Using a High-
- Throughput, Fully Automated Liquid-Handling Robotic System. SLAS Technol 25, 545–552
- 318 (2020).
- 319 29. Singh, L., Anyaneji, U.J., Ndifon, W. et al. Implementation of an efficient SARS-CoV-2 specimen
- pooling strategy for high throughput diagnostic testing. *Sci Rep* 11, 17793 (2021).
- 321 30. Zhang, Y. & Nguyen, N.-T. Magnetic digital microfluidics a review. Lab Chip 17, 994–1008
- 322 (2017).
- 31. Mibus, M. & Zangari, G. Performance and Reliability of Electrowetting-on-Dielectric (EWOD)
- 324 Systems Based on Tantalum Oxide. ACS Appl. Mater. Interfaces 9, 42278–42286 (2017).
- 32. Yu, W. et al. A ferrobotic system for automated microfluidic logistics. Sci Robot 5, (2020).
- 33. Dao Thi, V. L. et al. A colorimetric RT-LAMP assay and LAMP-sequencing for detecting SARS-
- 327 CoV-2 RNA in clinical samples. Sci. Transl. Med. 12, (2020).
- 328 34. Ji, M. et al. Automated multiplex nucleic acid tests for rapid detection of SARS-CoV-2, influenza
- A and B infection with direct reverse-transcription quantitative PCR (dirRT-qPCR) assay in a
- 330 centrifugal microfluidic platform. RSC Advances vol. 10 34088–34098 (2020).

- 33. Yu, L. *et al.* Simultaneous detection of SARS-CoV-2 and pandemic (H1N1) 2009 virus with realtime isothermal platform. *Heliyon* 7, e07584 (2021).
- 333 36. Mancini, F. *et al.* Multiplex Real-Time Reverse-Transcription Polymerase Chain Reaction Assays 334 for Diagnostic Testing of Severe Acute Respiratory Syndrome Coronavirus 2 and Seasonal 335 Influenza Viruses: A Challenge of the Phase 3 Pandemic Setting. *J. Infect. Dis.* 223, 765–774
- 336 (2021).
- 337 37. Stambaugh, A. *et al.* Optofluidic multiplex detection of single SARS-CoV-2 and influenza A antigens using a novel bright fluorescent probe assay. *Proc. Natl. Acad. Sci. U. S. A.* **118**, (2021).
- 38. Peeling, R. W., Olliaro, P. L., Boeras, D. I. & Fongwen, N. Scaling up COVID-19 rapid antigen tests: promises and challenges. *Lancet Infect. Dis.* **21**, e290–e295 (2021).
- 341 39. Dorfman, R. The Detection of Defective Members of Large Populations. *The Annals of Mathematical Statistics* vol. 14 436–440 (1943).

343 Figures and captions

344 Figure 1:

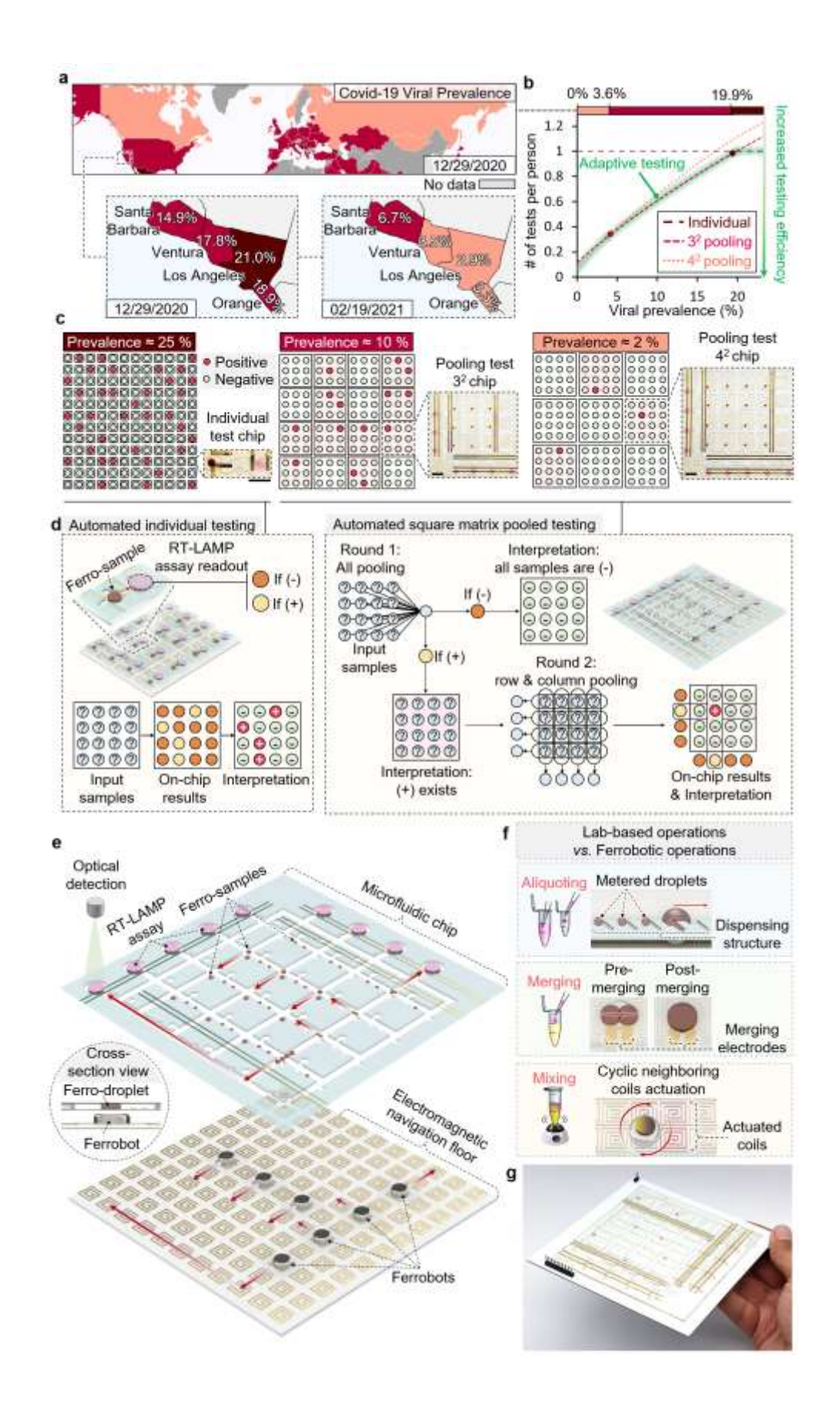


Fig. 1: Overview of the bioanalytical swarm ferrobotic platform for accessible, adaptable, and automated viral testing. a, Illustration of spatio-temporal varying COVID-19 viral prevalence (based on the test positivity rate data from Our World in Data and California Health and Human Services Open Data Portal). b, The required number of tests per person to find all infected people (across different levels of local viral prevalence), based on the square matrix pooled testing strategy. Green-highlighted curve illustrates that maximal screening efficiency can be achieved *via* adaptive (prevalence-based) testing. c, Illustration of the optimal testing modes and the associated ferrobotic chips (scale bar: 1 cm) for the representative local viral prevalence levels of 25%, 10%, and 2%. d, Schematic overview of the automated workflows for individual and pooled testing of 16 samples. e, Exploded schematic of a representative ferrobotic viral testing platform (*e.g.*, 4² pooling). f, Schematic illustrations of the ferrobotic equivalents of lab-based NAAT liquid handling operations, including aliquoting, merging, and mixing. g, Optical image of a representative ferrobotic viral testing platform for 4² pooled testing.

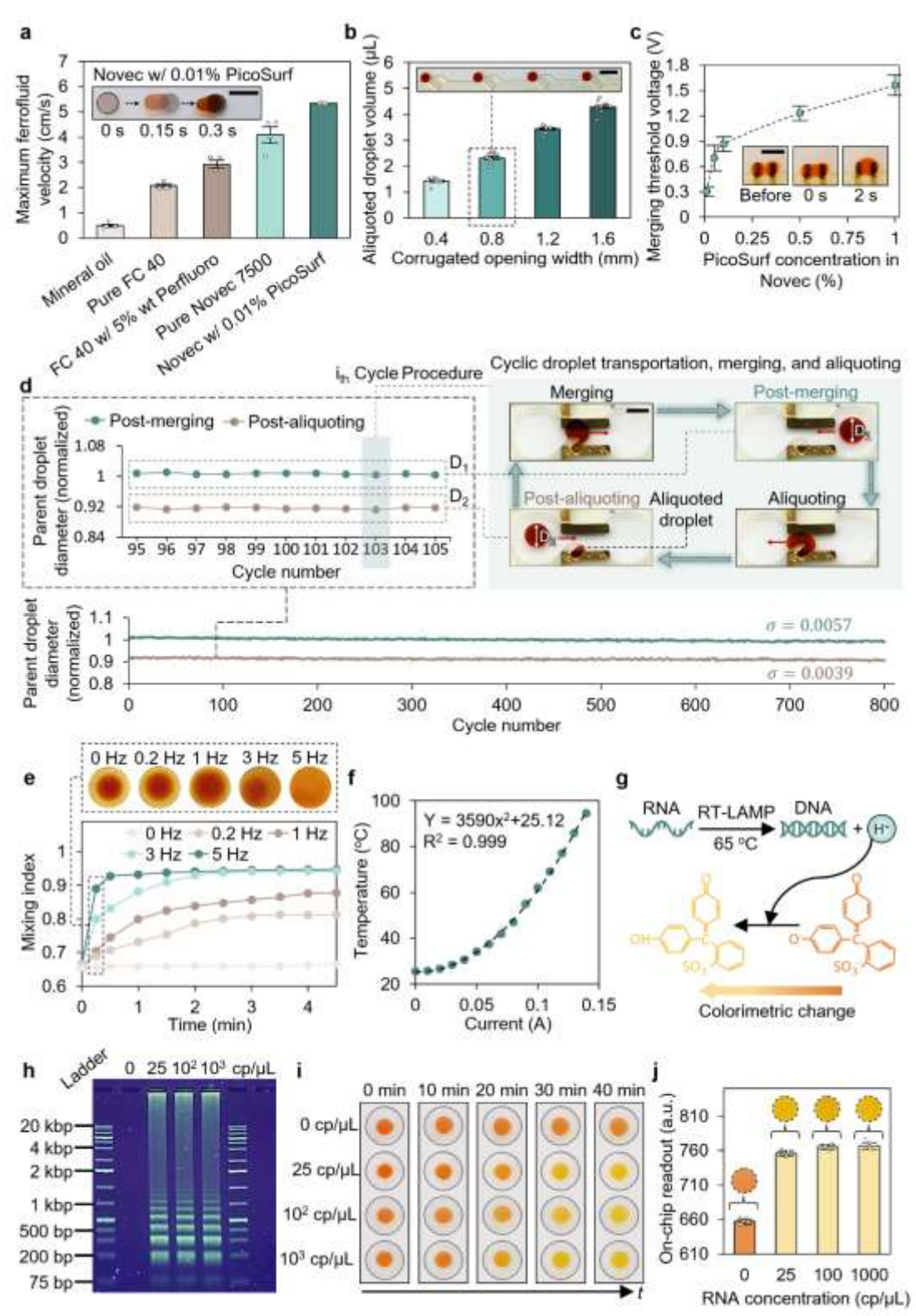


Fig. 2: Ferrobotic operations enable NAAT-based testing. a, Characterization of maximum ferro-droplet transportation velocity within different oil environments. Inset shows overlaid sequential images, visualizing

379

the transportation process (scale bar: 3 mm). Error bars, mean values \pm SE (n = 4 independent experiments). b, Characterization of the aliquoted droplet size for different corrugated opening widths (channel height: ~900 µm). Inset shows multiple aliquots of the same ferro-droplet source can be produced by extending the corrugated feature in an array format (scale bar: 5 mm). Error bars, mean values \pm SE (n = 12 across 3 replicates). c, Characterization of the threshold voltage for droplet merging using different concentrations of a surfactant (PicoSurf) within an oil (Novec) environment. Inset shows sequential optical images of the merging process (scale bar: 5 mm). Error bars, mean values \pm SE (n=3 independent experiments). d, Characterization of the cyclic ferrobotic operations, involving aliquoting, merging, and intermediate transportation of a parent droplet to evaluate the robustness of the ferrobotic operations (performed for > 800 cycles, scale bar: 3 mm). Parent droplet size varied by < 1% for each of the post-merging and post-aliquoting states (characterized optically). e. Progressive mixing index for different actuation frequencies. Top: corresponding images of the merged droplets under mixing at different actuation frequencies for 15 s. f, Characterization of the local temperature set by an on-board resistive heater for different input current. g, Schematic of the RT-LAMP reaction and detection mechanism. h, Representative gel electrophoresis analysis of the RT-LAMP reaction product (repeated 3 times, reaction period: 30 min). i, j, Sequential optical images (i) and on-chip readouts (j) of the RT-LAMP assay performed in ferro-droplets containing negative control and spiked SARS-CoV-2 positive control RNA (25, 100, 1000 cp/µL) samples. Error bars, mean values \pm SE (n = 10 independent optical sensor readouts).

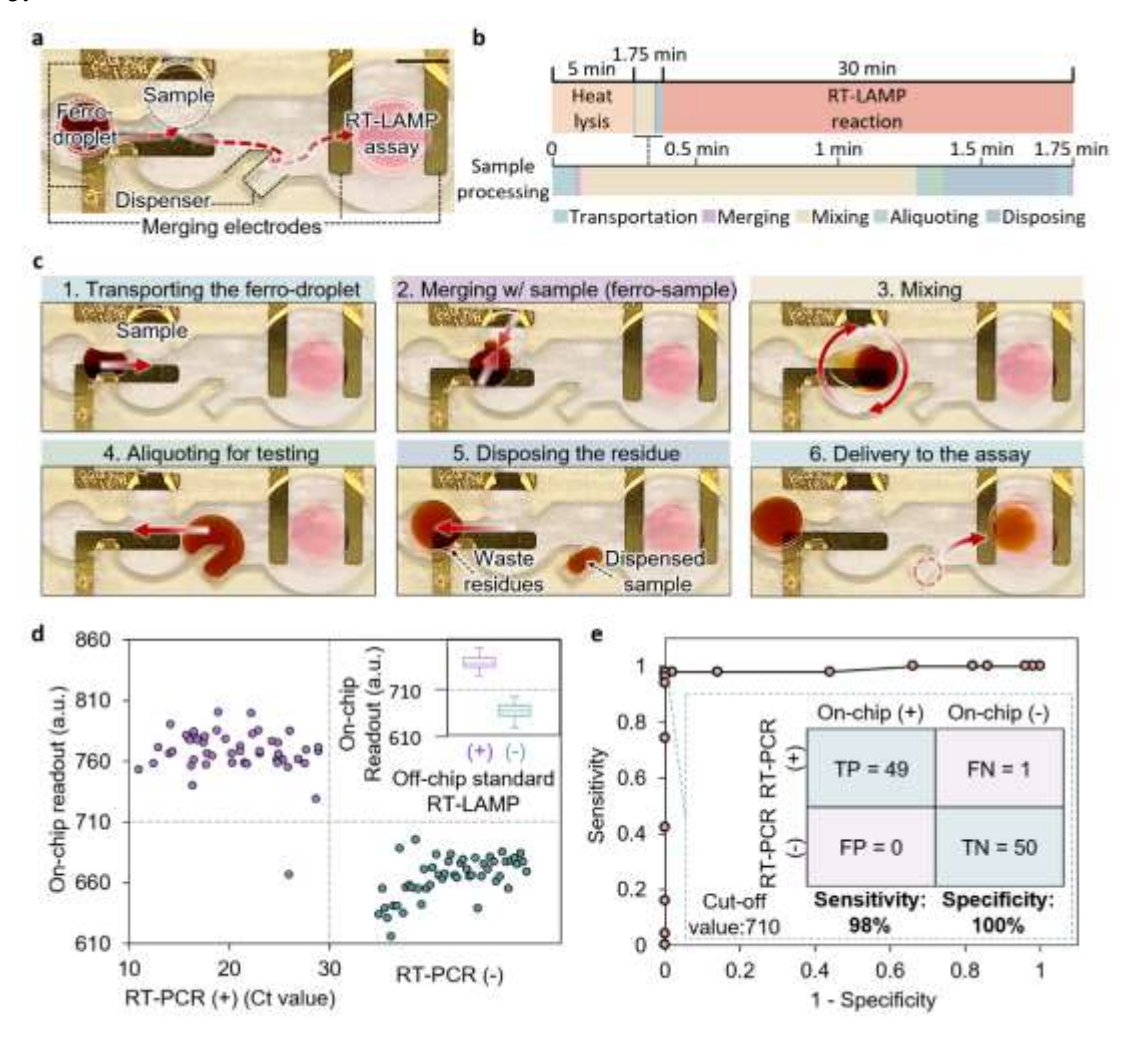


Fig. 3: Performance of an automated ferrobotic SARS-CoV-2 RT-LAMP workflow for individual clinical sample testing. a, Annotated image of the microfluidic chip for individual sample testing (scale bar: 5 mm). b, The timeline of the streamlined on-chip operations for automated individual testing, which includes active ferrobotic sample processing operations over a time window of 1.75 min. Heat lysis and RT-LAMP reaction are correspondingly performed at 95 and 65 °C. c, Sequential optical images of the active ferrobotic sample processing operations (performed automatically). d, Comparison of the ferrobotic SARS-CoV-2 RT-LAMP assay readouts with the corresponding RT-PCR results (Ct values) for a collection of one hundred clinical samples. Each datapoint represents one sample. Inset compares ferrobotically-produced vs. manually-performed RT-LAMP assay results, illustrating that the corresponding sample test results are in complete agreement (whisker limits show extremums, box limits show quartiles, the horizontal line is the median, for the same collection of n = 100 samples). e, Corresponding ROC curve of the analyzed samples. The sensitivity and specificity are based on the set cut-off value of 710 a.u. (also serving as the on-chip detection threshold).

Figure 4:

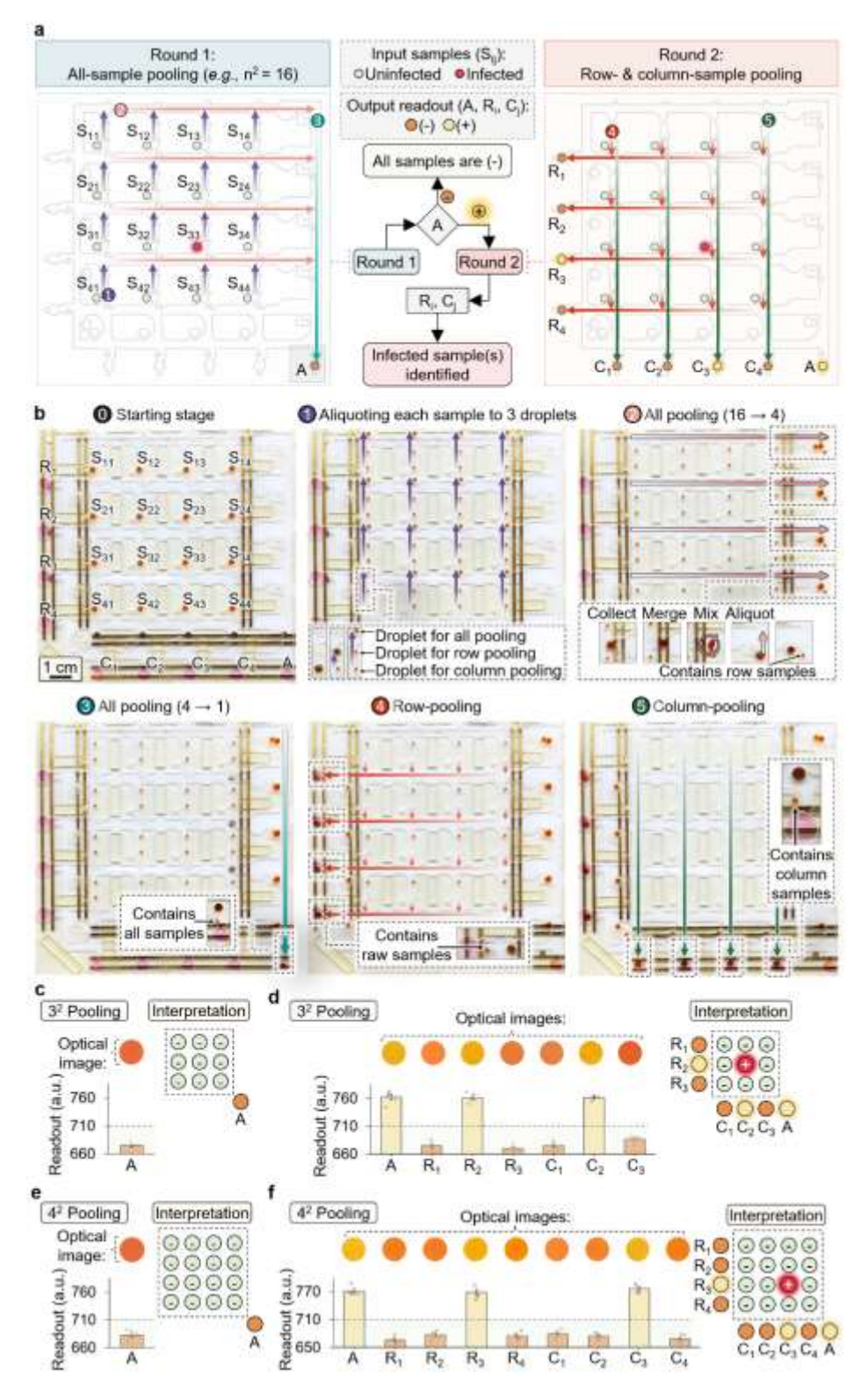


Fig. 4: Performing a pooled SARS-CoV-2 RT-LAMP workflow using a ferrobot swarm. a, Schematic of the square matrix pooling scheme. The flow chart at the center provides an overview of the infected sample identification process based on the assay pooled (A) or row/column (R_i/C_i) responses. b, Sequential optical

images of an automated 4^2 pooling workflow performed by a team of nine ferrobots. To combine aliquots in each pooling step, they are ferrobotically collected, merged, mixed, and then dispensed as a 1- μ L droplet. Inset images show the critical intermediary ferrobotic operations. **c**, **d**, Optical images and readouts obtained from ferrobotic pooled testing of two groups of 9 clinical samples using the 3^2 pooling chip. The negative assay A response indicated no infected sample was present among the first group of samples in (**c**). The positive assay A response along with the positive assay R_2 and C_2 responses led to the identification of the infected sample (located at the 2^{nd} row/ 2^{nd} column) among the second group of samples (**d**). **e**, **f**, Optical images and readouts obtained from ferrobotic pooled testing of two groups of 16 clinical samples using the 4^2 pooling chip. The negative assay A response indicated no infected sample was present among the first group of samples in (**e**). The positive assay A response along with the positive assay R_3 and R_4 responses led to the identification of the infected sample (located at the R_4 row/ R_4 column) among the second group of samples (**f**). Error bars indicate different trials of optical reading, mean values R_4 SE (R_4 = 5).

Materials and Methods

Materials and reagents for ferrobotic platform and viral testing

The ferrofluid used in this work is ferumoxytol, a U.S. Food and Drug Administration-approved intravenous iron preparation (AMAG Pharmaceuticals, MA, USA). Rare earth permanent magnets (D101 and DH2H2, with corresponding thickness/diameter of 0.8 mm/2.54 mm and 5 mm/5 mm) were purchased from K&J Magnetics (PA, USA) for device construction and characterization. The microfluidic module is constructed from double-sided tape (3M, 300LSE, MN, USA) and transparent PET film layers (M.G. Chemicals, Ontario, Canada). The microfluidic devices were filled with Novec 7500 Engineered oil (3M, MN, USA) containing 0% to 0.1% surfactant (Pico-Surf 1, Sphere Fluidics, NJ, USA), unless stated otherwise. Other oils including mineral oil (Sigma-Aldrich, MO, USA), FC-40 and corresponding surfactant (1H,1H,2H,2H-Perfluoro-1-decanol, Sigma-Aldrich, MO, USA) were also used for velocity characterization. Single stranded RNA (ssRNA) fragments of SARS-CoV-2 (108 copies/uL) were purchased from Sigma-Aldrich. Living E.coli K-12 strain (3×10⁵ CFU/μL) in liquid nutrient broth was purchased from Carolina Biological Supply (NC, USA). A SARS-CoV-2 Rapid Colorimetric RT-LAMP Assay Kit was purchased from New England Biolabs (NEB, MA, USA) and stored at -20°C. The Viral Transport Media (VTM) was purchased from BD (NJ, USA). The UCLA Clinical Microbiology Laboratory performed RT-PCR using the following assay: TaqMan COVID-19 RT-PCR Assay (ThermoFisher Scientific, Carlsbad, CA, USA).

Electromagnetic (EM) navigation floor circuit design

To manipulate ferrobots across 2D space, an EM navigation floor on PCB comprised active coil elements in a 2D-array format. Each element had a three-turn coil with a size of 1.5 mm by 1.5 mm traced onto the three layers of the PCB, with a 0.1 mm gap separated from adjacent elements. Each coil element can be activated by a 0.2 A direct current (DC), generating a localized magnetic force that attracts the ferrobot. Programmable current source ICs LT3092 (Linear Technology, CA, USA) were used to power the actuated coils (3 V, 0.6 W for each actuated coil). Programmable switch ICs MAX14662 (Maxim Integrated, CA, USA) were used to selectively activate the EM coils and components.

To enable scalable asynchronous parallel testing of 32 samples, the individual testing navigation floor comprised an array of 4 × 8 testing units. Each testing unit included two 20 Ohm resistive heaters, an array of 14 EM coils, and an optical sensing module containing a white-light LED (20 mA) and an ambient light sensor (3.3 V) with 560 nm peak absorbance (BH1721, ROHM Semiconductor, Japan). The optical components are operated with stable supply conditions, minimizing signal drift.

Each EM coil element was individually addressed by the output of a switch IC. The matrix-format navigation floor was designed for general ferrobotic operations and testing applications, comprising an active matrix array of EM coil elements, which was specifically selected when switch ICs activate corresponding rows and columns in the navigation floor (Extended Data Fig. 4f). Switch ICs were controlled *via* Serial Peripheral Interface (SPI) by an Arduino Nano, which in turn communicated with a computer through serial communication. Target coordinates preprogrammed or sent from the user interface were translated to SPI commands by the Arduino and then transmitted to switch ICs for addressable activation of the EM coils. The EM navigation floor can be functionalized with benchtop instruments (laptop and power supplies) or as a self-sufficient battery-operable handheld unit (Supplementary Fig. 9, Supplementary Video 4).

Microfluidic device fabrication

The microfluidic chips were fabricated by assembling layers of double-sided tape and transparent polyethylene terephthalate (PET) film sheets. In particular, one and six layers of double-sided tape were used to construct microfluidic chips with corresponding heights of ~150 µm and 900 µm. Patterns were laser cut into the double sided-tape and PET to make micro-channels (VLS 2.30, Universal Laser System, AZ, USA). The double-sided tapes and PET sheets were then thoroughly cleaned by immersing them in an acetone ultrasonic bath for 5 min, followed by repeating this cleaning process with isopropyl alcohol and deionized water. To completely dry the cleaned microfluidic layers, the devices were baked at 65 °C for 4 h. In order to make the surface of the microchannels hydrophobic, the inner surface of double-sided tape and PET sheets were exposed by a shadow mask and treated with NeverWet base-coat spray (Rust-Oleum, IL, USA), followed by resting for 30 min. The devices were then again treated with NeverWet top-coat spray, followed by room temperature incubation for 12 h. The droplet merging electrodes were patterned on PET sheets by photolithography using positive photoresist (AZ5214E, MicroChemicals, Germany), followed by the evaporation of 20 nm of Cr and 100 nm of Au and a lifting-off step in acetone. The fabricated microfluidic devices were preloaded with oils containing various concentrations of surfactants and reagents for experiments.

Maximum transportation velocity characterization within different oil environments

Microfluidic devices with 50-mm by 30-mm by 0.7-mm inner chambers were fabricated and assembled. A ferrobot was placed on top of the navigation floor and below the microfluidic device. Microfluidic chambers filled with different oils including mineral oil, FC-40 (w/ or w/o 5% Perfluoro) or Novec-7500 (w/ or w/o 0.01% Pico-Surf) were used for velocity characterization. After the ferrofluid droplets (2 μ L) were loaded in the microfluidic chambers, these droplets moved along with the ferrobot, which was sequentially guided

by the EM coils actuation in an array from left to right. The velocity of the ferrobot was controlled by adjusting the time interval between activating two adjacent coils. If the ferrofluid droplet followed the ferrobot to the end successfully, then the velocity of the magnet would increase by shortening the actuation time interval (by 1 ms) in the next round until the droplet failed to follow the magnet.

Droplet aliquoting characterization setup and procedure

To validate the aliquoting operation in the optimized oil environment, microfluidic devices (with heights of ~150 μ m or 900 μ m) containing various corrugated wall structures were designed. Devices with different opening widths (0.2, 0.4, 0.8, 1.2, and 1.6 mm) at the corrugated wall were fabricated, assembled, and tested. After a parent ferrofluid droplet was loaded in each device (2 μ L and 10 μ L for devices with channel heights of 150 μ m and 900 μ m, respectively), it was transported by the ferrobot along the same-sized repeated corrugated structures to aliquot smaller ferro-droplets. The aliquoted droplets were imaged to measure the droplet size.

Merging characterization setup and procedure

A microfluidic device for merging and mixing was fabricated and assembled, with patterned electrocoalescence electrodes (1 mm width, spaced 2 mm apart, thicknesses of 20 nm of Cr and 100 nm of Au) on PET substrate. To characterize merging, after two 5 μL ferrofluid droplets were loaded in each microfluidic device filled by Novec 7500 with different Pico-Surf surfactant concentrations (0.01%, 0.05%, 0.1%, 0.5%, 1%), the two droplets were manipulated by the ferrobot to the vicinity of the actuation electrode. A gradually increased (0.1 V increments) DC voltage was applied between the two electrodes until the droplets merged.

Mixing characterization setup and procedure

To characterize active mixing, the device was loaded with one 5 μL colored ferrofluid droplet and one 5 μL transparent water droplet. After merging, the underlying ferrobot was directed to induce chaotic fluid motion within the merged droplet with different frequencies (0.2, 1, 3, 5 Hz). A video recording was taken for the mixing process, and the droplet homogenization rate was calculated through image processing. To quantify mixing efficiency, the video frames were imported into—a MATLAB, and the pixel data (in grayscale) at the droplet region were extracted. A mixing index is defined, as expressed below:

511 Mixing index =
$$1 - \sqrt{\frac{1}{N-1} \sum_{i=1}^{N} \frac{(c_i - c_{ave})^2}{c_{ave}^2}}$$

where N, c_i , and c_{ave} are the total number of pixels, the grayscale values at pixel i, and the average grayscale values over N pixels, respectively.

Characterization of long-term cyclic ferrobotic operations

A microfluidic device that contains two chambers and a connection channel in between was fabricated and assembled. The connection channel contains a corrugated wall structure and a pair of merging electrodes deposited on the PET substrate. After a 7.0-μL ferro-droplet was loaded into the microfluidic chamber, the ferrobot manipulated the ferro-droplet periodically: dispense the droplet into mother and daughter droplets when transporting from the right chamber to the left chamber, and merge the mother droplet with the dispensed droplet when transporting from the left chamber to right chamber. These actions were repeatedly performed for more than 800 cycles. Images were taken during the whole process, and the dynamic variation of the droplet size was measured through image analysis. To illustrate the extreme reliability of the ferrobotic droplet actuation across different ionic strength and chemical conditions, 10 droplets with differing compositions (H₂O, PBS, 0.1 M and 1 M HCl, 0.1 M and 1 M KCl, 0.1 M and 1 M NaCl, 0.1 M and 1 M NaOH) were actuated by designated ferrobots over more than 70,000 cycles (12 commuted pixels-per-cycle/ferrobot) and 24 h. The actuation events and commuted pixels are tracked by monitoring the current through the designated impedance sensing gold electrode pairs (with the aid of CH Instrument 660E, TX, USA; applied voltage: 1 V).

Programmable heating characterization setup and procedure

To implement programmable heating, a microfluidic device was placed on the PCB that contained resistive heaters. The heated region in the chip was placed right above the location of the resistive heater. Copper cubic blocks (3 mm length, 0.8 mm width, 2 mm height) were placed between the PCB surface and microfluidic chip for heat transduction. To characterize the heating function, different current was applied through the resistive heater (0 - 0.14 A), inducing a temperature increase by Joule heating. The temperature was then measured by a thermocouple. By programming the current through the resistive heater, the local temperature can be set in relation to the surrounding temperature (Supplementary Fig. 2b,c). If increased precision control of local temperature is desired, a temperature sensor can be integrated to form an internal real-time closed-loop temperature control mechanism.

Off-chip RT-LAMP characterization

To detect RNA, RT-LAMP assays were conducted at room temperature. As the standard protocol described by NEB, every 25 μL RT-LAMP assay included 12.5 μL WarmStart Colorimetric RT-LAMP 2X master mix, 2.5 μL guanidine hydrochloride, 2.5 μL target RNA primer mix, 5.5 μL nuclease-free water, and 2 μL input sample. To characterize the RT-LAMP assay for SARS-CoV-2 detection, ssRNA fragments of SARS-CoV-2 diluted to various concentrations (0, 25, 100, 1000 copies/μL) were mixed with the assay as input

sample, then the RT-LAMP assays were incubated at 65 °C for 30 minutes. After incubation, the assays were further analyzed by Nanodrop One (Thermo Fisher Scientific, MA, USA) and gel electrophoresis. Plate reader Cytation 5 (BioTek, VT, USA) was also used to record the assay absorbance (at 560 nm) during incubation (at 65 °C) using a 384 well plate.

RT-LAMP characterization within the ferrobotic chip

To characterize the RT-LAMP assay performance within the ferrobotic chip, a 20 μL-RT-LAMP assay containing ferrofluid was prepared for on-chip reaction. The compositions of the assay are: 10 μL WarmStart Colorimetric RT-LAMP 2X master mix, 2 μL guanidine hydrochloride, 2 μL target RNA primer mix, 5 μL nuclease-free water and 1 μL input sample. The input sample contained ssRNA fragments of SARS-CoV-2 in various concentrations (0, 25, 100, 1000 copies/μL) and 13% of ferumoxytol. The RT-LAMP assays were loaded in the testing microfluidic device and incubated at 65 °C for 30 minutes. The incubation process of the assay was recorded by video. After the RT-LAMP reaction, the color was quantitatively measured by the optical sensing module. Similar procedure was performed with a 2 μL-RT-LAMP assay and using microfluidic devices with reduced height (~150 μm), when characterizing the assay's response to 100 nL-input samples.

Standard RT-PCR test for clinical samples

The TaqPath COVID-19 RT-PCR assay targets the SARS-CoV-2 S, N and ORF1ab genes. Extraction was performed on the automated KingFisher Flex Purification System. RT-PCR was performed on the Applied Biosystems 7500 Real-Time PCR Instrument. Detection of two or more targets was considered positive. All testing was performed on nasopharyngeal swabs collected from symptomatic patients. The CT values were extracted from each instrument and represent a midpoint between the target genes.

Off-chip RT-LAMP detection for clinical samples

All clinical samples were obtained following University of California, Los Angeles, Institutional Review Board Approval (IRB#21-000982). Clinical samples were collected using a nasal swab, stored in the VTM at -80°C, and added into PBS buffer (20% VTM + 80% PBS buffer) with inactivation reagent (including 6 mM NaOH for adjusting pH, 2.5 mM TCEP-HCl, 1 mM EDTA). For the off-chip RT-LAMP test, the samples were placed in a heat block set to 95 °C for 5 min to be inactivated. RT-LAMP assays were prepared following the off-chip protocol and incubated at 65 °C for 30 minutes. Optical images were taken after the incubation.

Ferrobotic individual clinical sample testing

To perform ferrobotic SARS-CoV-2 individual tests on clinical samples, microfluidic devices containing a sample input chamber, a ferrofluid chamber, an assay chamber, two pair of merging electrodes (patterned at the sample input chamber and assay chamber) and a dispensing structure was fabricated and assembled. Each microfluidic chip was preloaded with a ferrofluid droplet (50% ferumoxytol) in the ferrofluid chamber and RT-LAMP assay solution in the assay chamber (reagent volume: $1.9~\mu L$ and $19~\mu L$ for analysis of 100-nL and $1~\mu L$ -aliquoted samples, respectively). For clinical sample analysis, the starting sample was pipetted into the microfluidic chip at the sample input chamber (via the designated sample inlet). Specifically, $0.52~\mu L$ and $5.2~\mu L$ of starting samples were correspondingly used for subsequent aliquoting/analysis of 100-nL and $1~\mu L$ droplets. Then heat inactivation and lysis was were performed on the PCB for 5 minutes by powering a 20-Ohm resistive heater with 0.14~A~DC current. Thereafter, a ferrobot performed the sample processing steps of transportation, merging, mixing, aliquoting, disposal, and delivery to the assay. Then, the on-chip RT-LAMP reaction (at $65~^{\circ}C$) continued for 30 min. The assay readout was measured by the optical sensing module.

Ferrobotic multiplexed testing

For multiplexed detection of SARS-CoV-2, influenza A–H1N1, and rActin RNA, a microfluidic device with a sample input chamber, a ferrofluid chamber, an assay chamber array, two pairs of merging electrodes (patterned at the sample input chamber and across the assay chamber array), and a dispenser array was fabricated and assembled. Each microfluidic chip was preloaded with a ferrofluid droplet in the ferrofluid chamber and three 19-µL RT-LAMP reaction solutions, containing primers for SARS-CoV-2, influenza A–H1N1 (Thermo Fisher Scientific, MA, USA), and internal control (NEB, MA, USA) respectively, in the assay chamber array. When performing a validation test, a blank sample or negative nasal swab sample either with or without target (spiked with SARS-CoV-2 and/or influenza A–H1N1 positive control) was loaded into the microfluidic chip at the sample input chamber. Inactivation/lysis was then performed on the PCB for 5 minutes by powering a 20-Ohm resistive heater with 0.14 A DC current. Thereafter, a ferrobot performed the sample processing steps of transportation, merging, mixing, aliquoting, disposal, and delivery to the assays. Each RT-LAMP assay solution ended up receiving a 1 µL ferro-sample. Then, the on-chip RT-LAMP reaction (at 65 °C) continued for 30 min. The readout for each assay was measured by the optical sensing module.

Ferrobotic pooled clinical sample testing

For pooled tests of clinical samples, microfluidic devices with a matrix array of sample input chambers, dispensers, two arrays of assay chambers and five pairs of merging electrodes (patterned across the assay

well arrays and mixing regions) were fabricated and assembled. The assay chambers were preloaded with RT-LAMP assay solutions (reagent volume: 1.9 μ L and 19 μ L for 100-nL and 1 μ L-aliquoted samples, respectively). A number of 3.5- μ L heat-inactivated starting ferro-samples were loaded into the input chambers (9 for 3², 16 for 4² pooling testing). Thereafter, ferrobots performed the sample processing steps of several rounds of aliquoting, transportation, merging, mixing, and delivery to the corresponding assay chambers. The navigation planning of the ferrobots accounted for the maintenance of an inter-ferrobot distance of 10 mm to avoid inter-ferrobot magnetic interference. The on-chip RT-LAMP reaction took place for 30 min (at 65 °C). The assay readout was measured by the optical sensing module.

RT-LAMP validation in diluted clinical sample

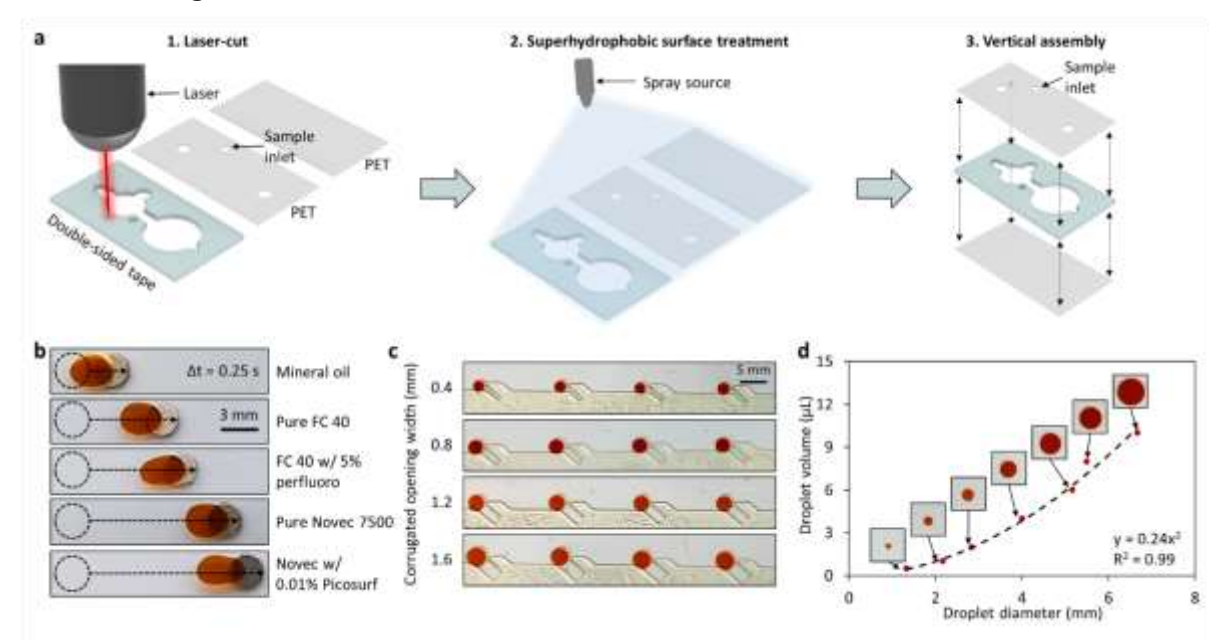
Five nasal swab samples (originally obtained from COVID-19 infected donors, pre-characterized *via* RT-PCR) with various Ct values (11, 15.7, 21.16, 24.97, and 28.95) were diluted in PBS with different dilution rates (4, 9, 16, and 25). Then, all the diluted and undiluted samples were tested by both standard off-chip RT-LAMP and on-chip RT-LAMP testing. The reaction products of standard off-chip RT-LAMP were visually recorded in tubes. The reaction products of on-chip individual RT-LAMP were visually recorded in the microfluidic chips, then quantitatively measured by the optical sensing module.

631	Data availability:
632	All data needed to evaluate the findings and conclusions in the paper are present in the paper and/or
633	Supplementary Information, and can be accessed through the Open Science Framework at
634	https://osf.io/ac9hz/?view_only=7b610238e37848faa05c89b7aa48e54a
635	(https://doi.org/10.17605/OSF.IO/AC9HZ).
636	
637	Acknowledgements:
638	We thank the UCLA Nanoelectronics Research Facility (NRF) for providing access to device fabrication
639	equipment. The authors also thank C. Zhang for discussions on EWOD fabrication. This work was
640	supported by S.E.'s startup package provided by the UCLA Henry Samueli School of Engineering and
641	Applied Sciences and UCLA W. M. Keck Foundation COVID-19 Research Award Program. Components
642	of research are supported by National Science Foundation (CAREER Award #1847729) and Precise
643	Advanced Technologies and Health Systems for Underserved Populations (PATHS-UP, NSF Engineering
644	Research Center, Award # 1648451, S.E., D.D.).
645	
646	Author information:
647	These authors contributed equally: Haisong Lin, Wenzhuo Yu, and Kiarash A. Sabet.
648	
649	<u>Affiliations</u>
650	Interconnected and Integrated Bioelectronics Lab (I2BL), Department of Electrical and Computer
651	Engineering, UCLA, CA, USA
652	Haisong Lin, Wenzhuo Yu, Kiarash A. Sabet, Yichao Zhao, Shuyu Lin, Sam Emaminejad
653	
654	Department of Bioengineering, UCLA, CA, USA
655	Michael Bogumil, Jacob Hambalek, Dino Di Carlo, Sam Emaminejad
656	
657	Department of Pathology and Laboratory Medicine, UCLA, CA, USA
658	Sukantha Chandrasekaran, Omai Garner
659	
660	Contributions
661	S.E., D.D., H.L., W.Y., and K.A.S. conceived the study idea and contributed to the design of experiments.
662	H.L., W.Y., and K.A.S. led the experiments with assistance from M.B., Y.Z., J.H., and S.L., H.L., W.Y.,
663	K.A.S., and Y.Z. conducted the device fabrication and characterization. H.L., W.Y., and K.A.S. designed
664	the PCB circuit. H.L., W.Y., K.A.S., M.B., S.C., and O.G. carried out the clinical studies. H.L., W.Y.,

665	K.A.S., M.B., and J.H. contributed to analytical tools and data analysis. S.E., D.D., H.L., W.Y., K.A.S.,
666	drafted the manuscript, and all the authors provided feedback.
667	
668	Corresponding authors
669	Correspondence to: Dino Di Carlo, Sam Emaminejad.
670	
671	Ethics declarations:
672	Competing interests
673	The authors declare the existence of a published patent publication No. 62/924,505, co-invented by some
674	of the co-authors (S.E., D.D, W.Y., H.L.).

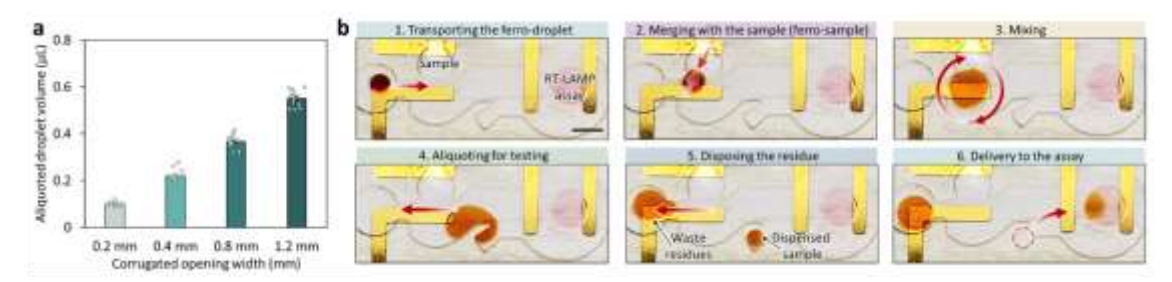
Extended data figures:

Extended Data Figure 1:

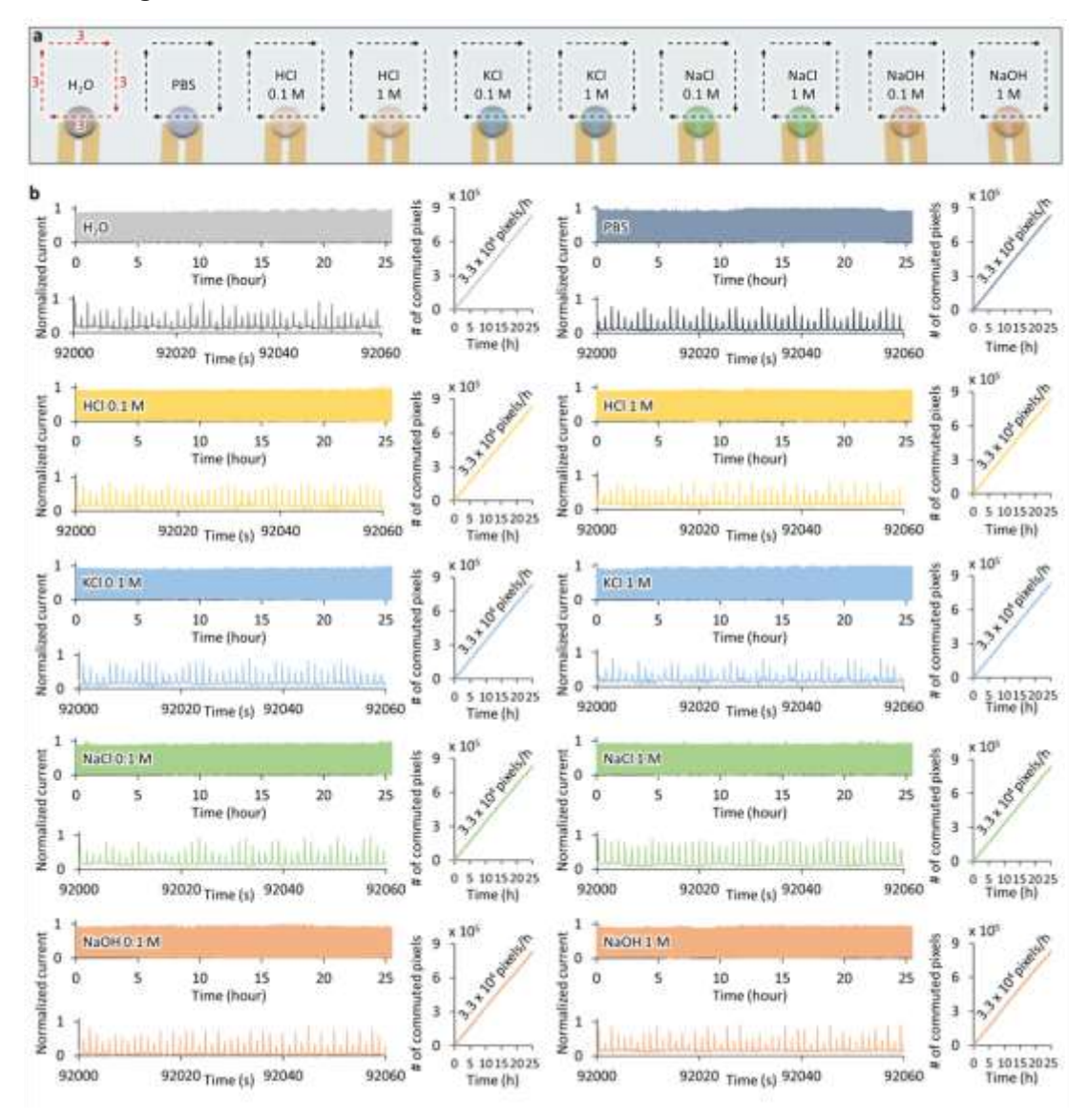


Extended Data Figure 1: Fabrication of microfluidic chips and characterization of ferrobotic operations. a, Fabrication process of the microfluidic chip (e.g., individual testing chip). b, Optical images of ferro-droplet-carrying ferrobots at $\Delta t = 0.25$ s, visualizing the maximum achievable transportation velocities within different oil environments. In all cases, the ferrobots are programmed to travel at the highest possible velocity that allows for the ferro-droplets to keep up with the underlying ferrobot movement. c, Optical images of the arrays of aliquoted droplets for different corrugated opening widths. d, Relationship between the ferro-droplet diameter and volume. Insets show optical images of the ferro-droplets.

Extended Data Figure 2:

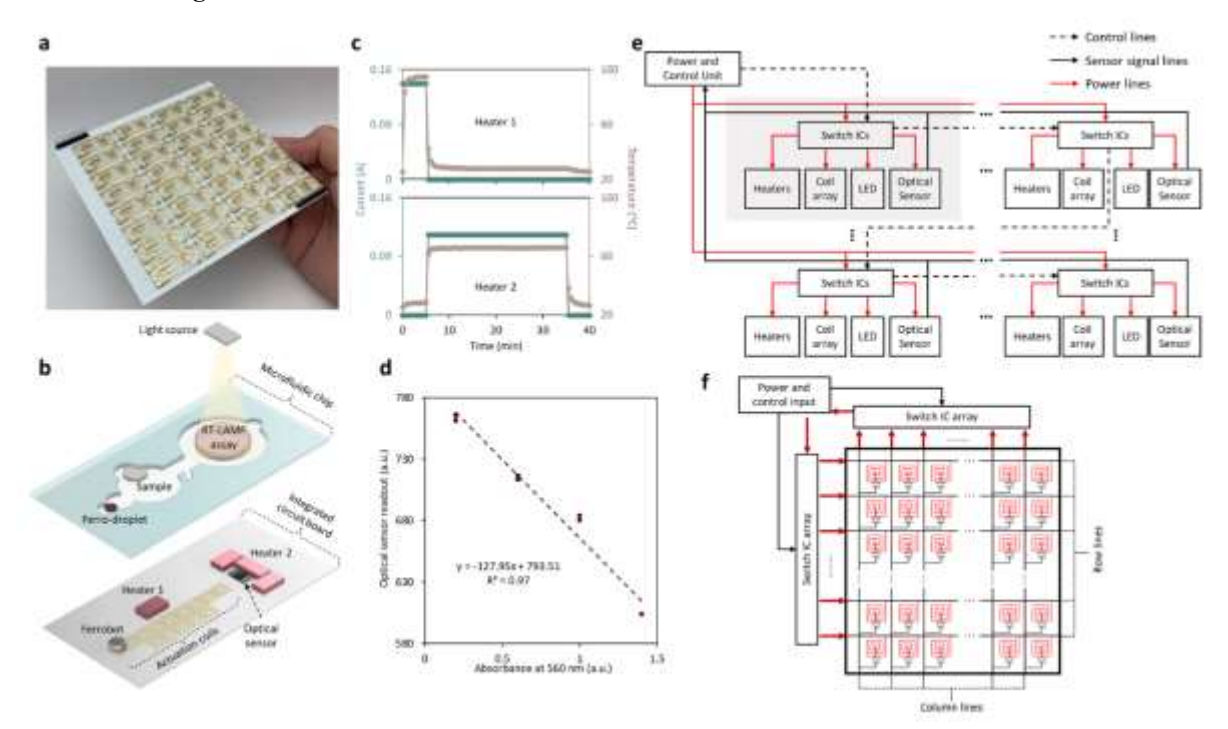


Extended Data Figure 2: Characterization and demonstration of ferrobotic operations in small sample volume device. a, Characterization of the aliquoted droplet volume for different corrugated opening widths (channel height: \sim 150 µm). Error bars, mean values \pm SE (n = 12 across 4 replicates). b, Sequential images of the active ferrobotic sample processing operations in a small sample volume device (dispensed sample \sim 100 nL; scale bar: 5 mm).



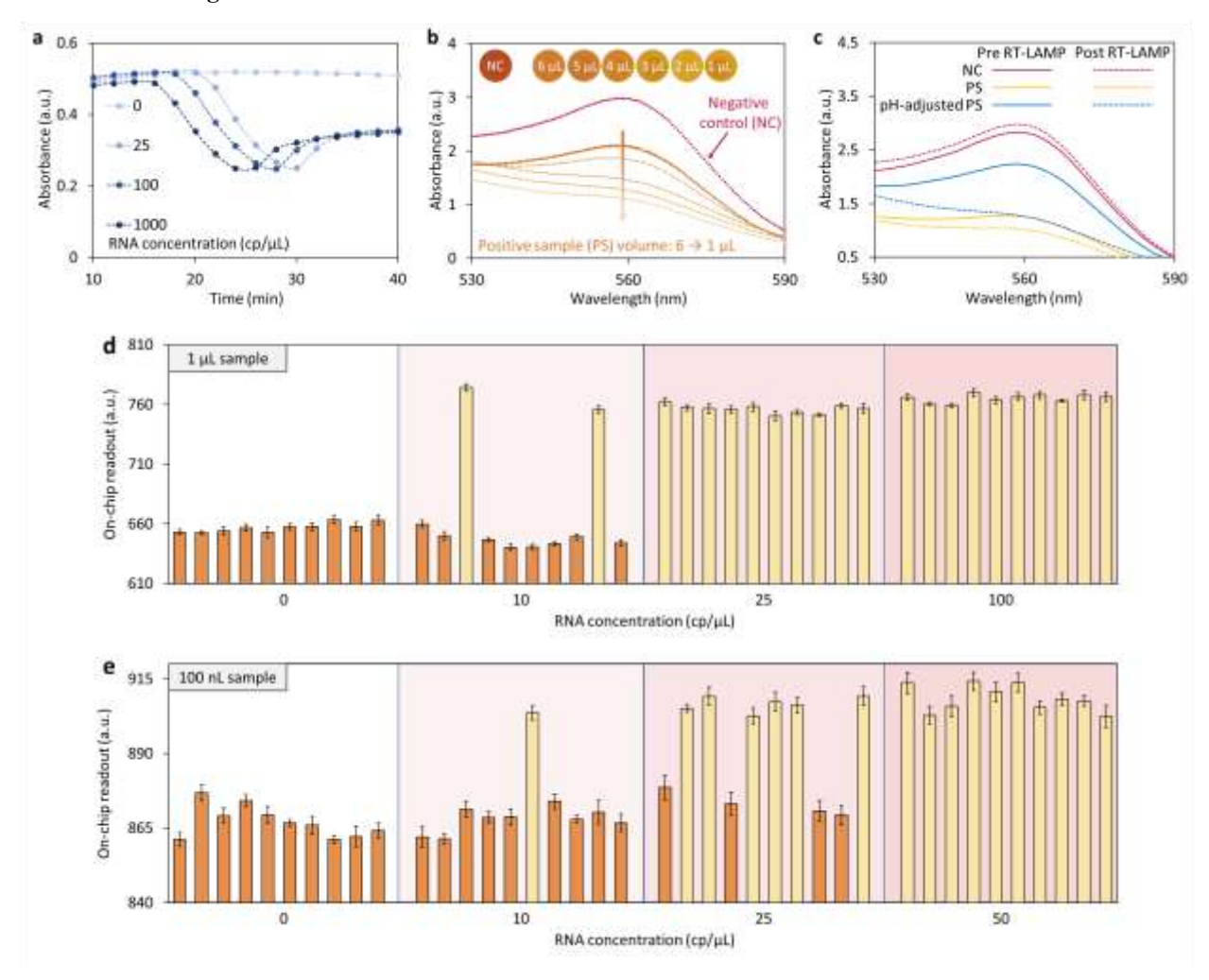
Extended Data Figure 3: Characterization of the robustness of ferrobotic actuation over a range of ferrodroplet ionic strengths and chemical conditions. a, Schematic of the characterized ferrobotic actuation, involving cyclic actuation of 10 ferro-droplets (with differing ionic strengths and chemical conditions) by designated ferrobots (12 commuted pixels-per-cycle/ferrobot). The actuation events and commuted pixels are tracked by monitoring the current through impedance sensing electrode pairs. b, Corresponding normalized measured current through the electrode pairs and accumulated commuted pixels over time (based on the recorded current peaks) are shown, resulting in a total of > 8 million actuation events over > 24 h (only limited by observation time).

Extended Data Figure 4:



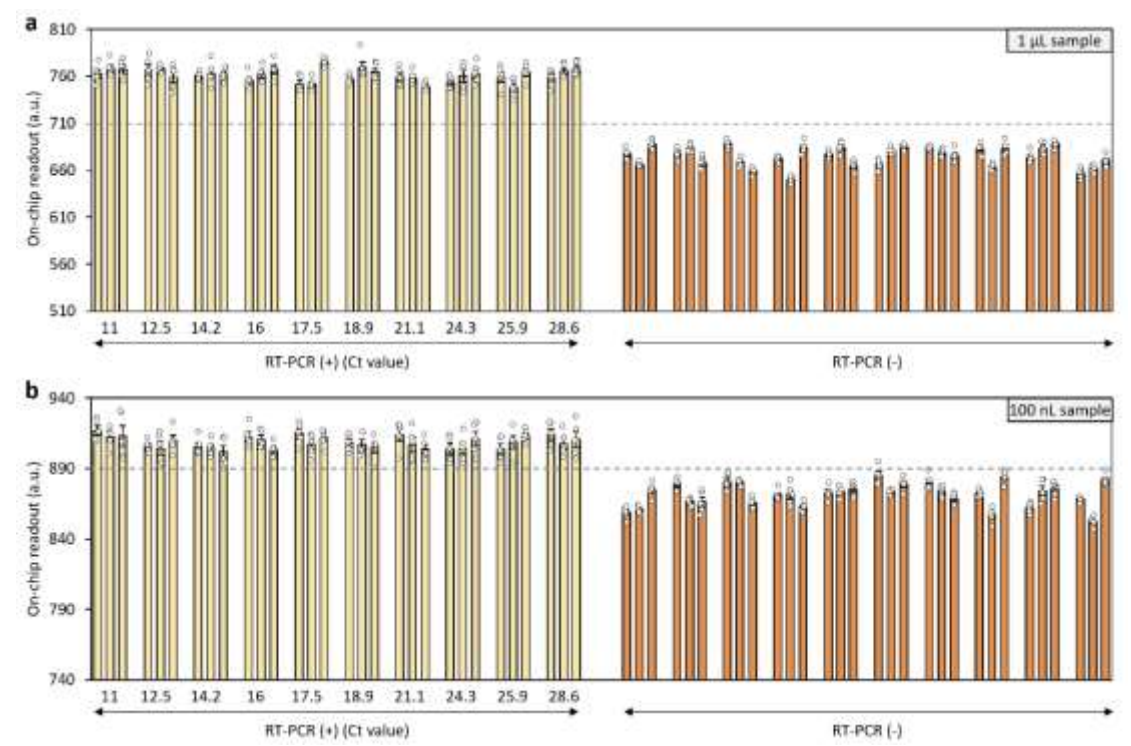
Extended Data Figure 4: Demonstration of fully integrated platform and component characterization. a, Optical image of a representative multi-sample ferrobotic platform for individual testing (here, 32 test sites). b, Exploded schematic of the microfluidic layer and actuation/sensing layer for a ferrobotic viral testing device designed for individual testing. c, Programmed input current profiles of two neighboring (12-mm apart) on-board resistive heaters and the correspondingly established local temperature profiles. d, Characterization of optical sensor readout *versus* standard Nanodrop readout (using solutions containing different concentrations of a pink color dye. Error bars, mean values \pm SE (n = 5 independent optical sensor readouts). e, Schematic diagram of the circuitry for a multi-sample individual testing PCB (extended into an array format). f, Schematic diagram of the control circuitry used for multiplexed testing (featuring an expanded coiled navigation floor).

713 Extended Data Figure 5:



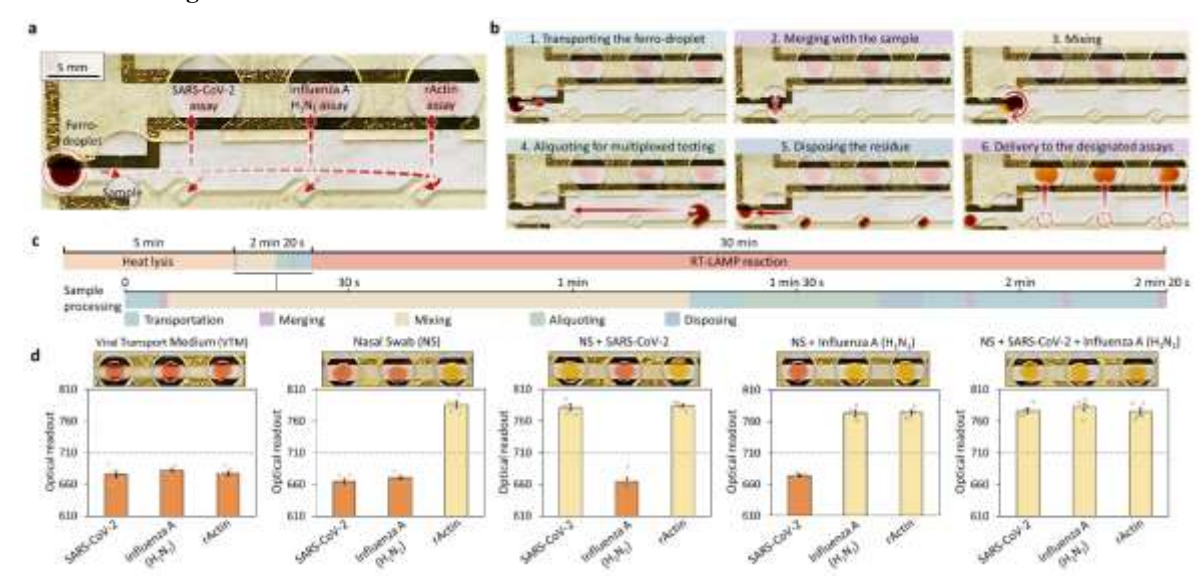
Extended Data Figure 5: Characterization of the colorimetric RT-LAMP assay. a, Quantification of the RT-LAMP assay response by real-time absorbance measurement using a plate reader. b, Absorbance spectra and corresponding optical images (insets) of the RT-LAMP reaction products for different volumes of positive input samples (6 to 1 μ L, reaction period: 30 min). c, Absorbance spectra of the RT-LAMP assay solution pre- and post-RT-LAMP reaction, showing the utility of the assay pH adjustment for optimizing the assay's colorimetric response. d, e, RT-LAMP colorimetric readout for ferro-droplet sample volumes of 1 μ L (d) and 100 nL. (e), across various input SARS-CoV-2 RNA copy numbers or negative controls (10 independent tests per condition). Limits of detection of 25 cp/ μ l and 50 cp/ μ l are observed for the 1 μ L and 100 nL sample respectively, likely limited by statistical sampling errors when copy number approaches ~1 per sample volume. Error bars, mean values \pm SE (n = 5 independent optical sensor readouts).

725 Extended Data Figure 6:



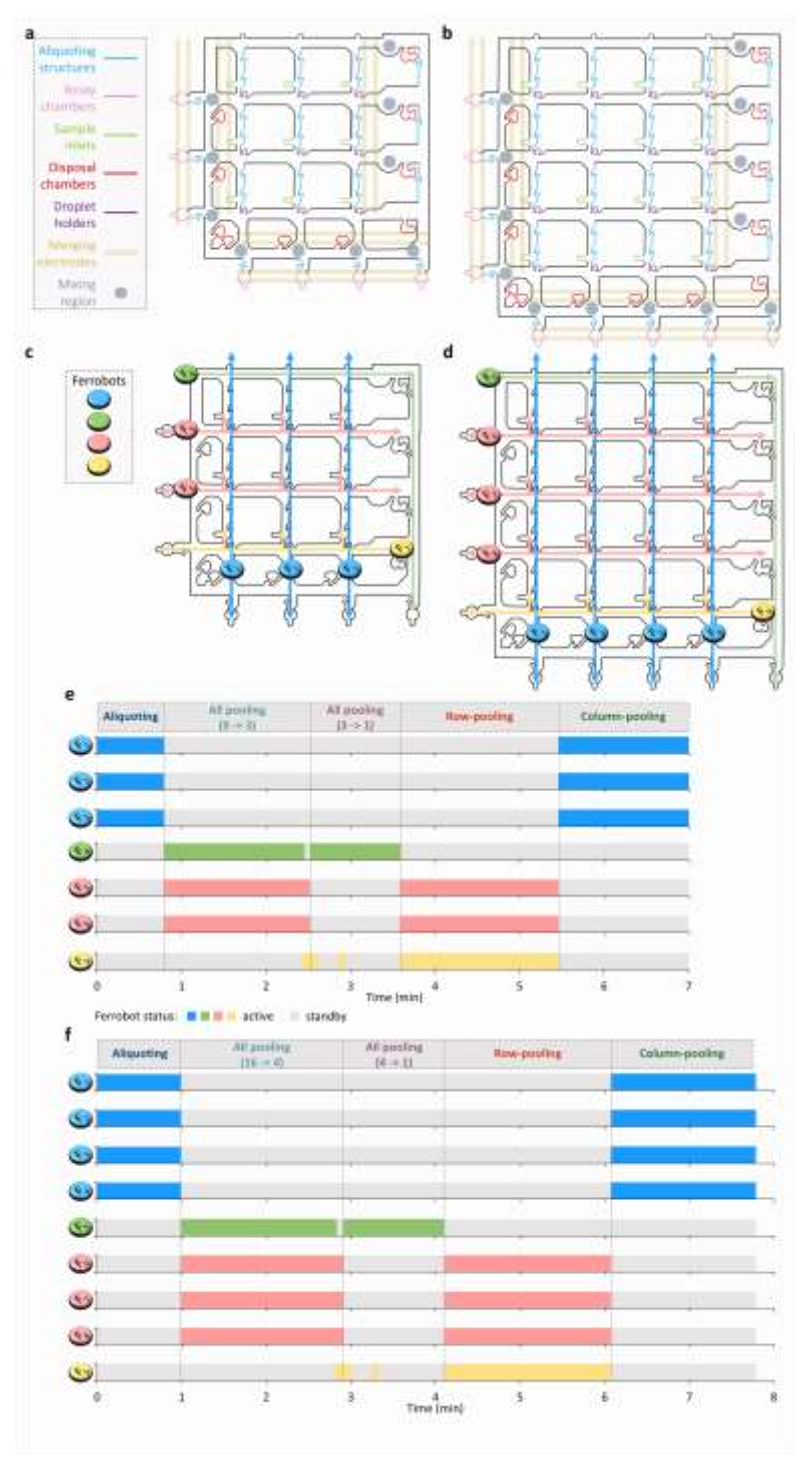
Extended Data Figure 6: Repeatability and reproducibility of ferrobotic tests with clinical samples. a, b, Ferrobotic SARS-CoV-2 RT-LAMP assay readouts corresponding to ferro-droplet sample volumes of 1 μ L (a) and 100 nL (b). Clinical samples from 10 SARS-CoV-2 infected and 10 uninfected patients (pre-characterized via RT-PCR) were analyzed across three replicates for each sample volume. Error bars indicate different repeats of colorimetric reading, mean values \pm SE (n = 5). The colorimetric detection threshold for positivity for the 1 μ L- and 100 nL-test sample volume cases is correspondingly 710 a.u. and 890 a.u. in our system.

733 Extended Data Figure 7:



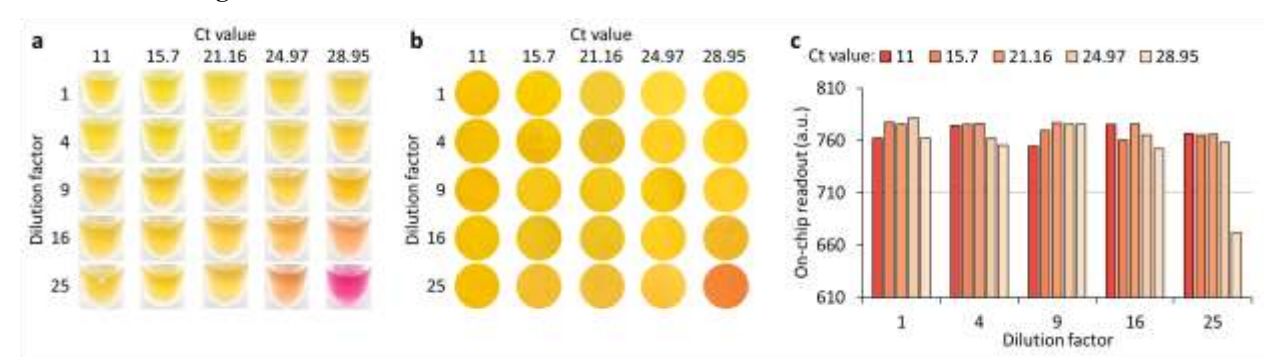
Extended Data Figure 7: Ferrobotically-automated RT-LAMP for multiplexed testing. a, Annotated image of the microfluidic chip for multiplexed testing. **b**, Sequential optical images of the active ferrobotic sample processing operations (performed automatically). **c**, The timeline of the streamlined on-chip operations for automated multiplexed testing, which includes active ferrobotic sample processing operations over a time window of 2:20 min:s. **d**, Optical images and corresponding on-chip readouts of the SARS-CoV-2, influenza A–H1N1, and rActin (internal control, IC) RT-LAMP assays for different combinations of input samples (spiked with corresponding RNAs). Nasal Swab (NS) samples naturally contain rActin. Error bars indicate different trials of optical reading, mean values ± SE (n = 5).

Extended Data Figure 8:



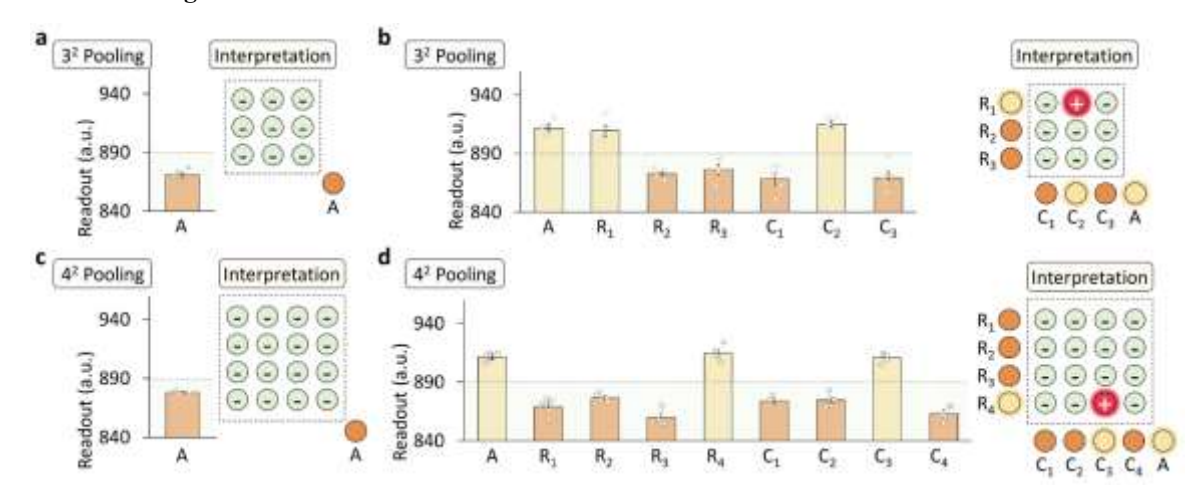
Extended Data Figure 8: Microfluidic chip layouts and the ferrobot navigation plans and task assignment for pooled testing. a, b, Schematic illustration of the microfluidic chip layout for 3^2 (a) and 4^2 (b) pooled testing (key features are outlined and labeled). c, d, Overview of the navigation plans of seven and nine ferrobots for 3^2 (c) and 4^2 (d) pooled testing. Each F_i represents an individual ferrobot. e, f, The timeline of the ferrobots' assigned tasks and status (active, standby) for 3^2 (e) and 4^2 (f) pooled testing.

749 Extended Data Figure 9:



Extended Data Figure 9: Detection of virus in diluted and undiluted clinical samples by colorimetric SARS-CoV-2 RT-LAMP assay. a, b, Optical images of the standard assay responses in microfuge tubes (a) and on-chip assay responses (b) for undiluted or diluted patient samples with different Ct values. c, Corresponding optical readouts of the on-chip assay responses.

756 Extended Data Figure 10:



Extended Data Figure 10: Pooled testing using 100 nL sample volumes. a, b, Readouts obtained from ferrobotic pooled testing of two groups of 9 clinical samples using the 32 pooling chip. The negative assay A response indicated no infected sample was present among the first group of samples in (a). The positive assay A response along with the positive assay R_1 and C_2 responses led to the identification of the infected sample (located at the 1^{st} row/ 2^{nd} column) among the second group of samples (b). c, d, Readouts obtained from ferrobotic pooled testing of two groups of 16 clinical samples using the 42 pooling chip. The negative assay A response indicated no infected sample was present among the first group of samples in (c). The positive assay A response along with the positive assay R_4 and C_3 responses led to the identification of the infected sample (located at the 4^{th} row/ 3^{rd} column) among the second group of samples (d). Error bars indicate repeated optical readings, mean values \pm SE (n = 5). Assays were performed in small volume microfluidic chips (channel height: $\sim 150 \mu m$; aliquoted sample volume: 100 nL; and reagent volume: $1.9 \mu L$).